

Pseudo-rapidity Distribution of Charged Particles in Relativistic Heavy Ion Collision

Kohta Haruna

Department of Physics Science
Graduate School of Science, Hiroshima University

February, 2006

Abstract

According to Quantum ChromoDynamics (QCD) theory, as the underlying theory of strongly interacting system, quarks and gluons are deconfined and can traverse freely out of the ordinary size of a nucleon under high temperature and/or dense condition. It is a hope that the relativistic heavy ion collisions may create the high temperature condition. If the deconfinement is interpreted as a state where the carriers of particle production are partons and these partons interact each other having a longer mean free path than size of a nucleon, it could be one of evidences of QCD deconfinement in a extreme condition.

A collision experiment of two gold nuclei at Relativistic Heavy Ion Collider (RHIC) at C.M.S. collision energy per nucleon pairs of 200GeV has been carried out at Brookhaven Notional Laboratory (BNL). The particles yielded by collisions are measured by particle tracking detectors and charged particle detectors using Cerenkov radiation. The multiplicity of primary charged particles is obtained as a function of pseudo-rapidity. The correction for detector efficiency and geometrical acceptance and the estimation of background contributed by secondary particles which are radiated except in the collision vertex is calculated by the simulation. Pseudo-rapidity is defined as a function of polar angles between primary charged particles and beam axis and is defined as $\eta = -\ln(\tan(\theta/2))$. With an assumption that pseudo-rapidity distribution is described by double Gaussian function, fits are performed to pseudo-rapidity distribution to interpolate and extrapolate the data points and to integrate in the whole pseudo-rapidity region. The total multiplicity of primary charged particles normalized to the number of nucleon pairs participating to a collision, compares with the results of e^+e^- and $pp/\bar{p}p$ collisions as a function of collision centrality and collision energy.

From the results of comparisons, it was found that total multiplicity in central Au+Au collisions scales with e^+e^- collisions rather than $pp/\bar{p}p$ collisions. In addition to that, above $\sqrt{s_{NN}} = 20\text{GeV}$, it was found that there were no leading parton effect in nucleus-nucleus collisions. In such collision energies, particle production in e^+e^- interaction is well described by a partonic picture. The scaling to e^+e^- of multiplicity means that the degree of freedom of partons appears in the particle production in nucleus-nucleus collisions. Absence of leading effect indicates the multiple interactions in nucleus-nucleus collisions, therefore particle interactions in high energy nucleus collisions are similar to the picture of deconfinement.

Contents

1	Introduction	5
1.1	Quark Gluon Plasma	5
1.2	Particle Production	6
1.3	Motivation of This Study	9
2	Experimental Setup	11
2.1	Relativistic Heavy Ion Collider	11
2.2	PHENIX Detector	13
2.2.1	Magnet	15
2.2.2	Beam Beam Counter	15
2.2.3	Zero Degree Calorimeters	17
2.2.4	Drift Chamber	19
2.2.5	Pad Chamber	19
2.2.6	Ring Imaging Cerenkov Hodoscope	20
2.2.7	Time Expansion Chamber	20
2.2.8	Time of Flight	20
2.2.9	Electro Magnetic Calorimeters	21
2.2.10	Muon Spectrometers	21
2.3	Trigger and Data Acquisition system	22
3	Data Analysis	25
3.1	Run Summary and Trigger Selection	25
3.2	Calibration	25
3.2.1	FEM Calibration	27
3.2.2	Gain Calibration	28
3.2.3	Time Calibration	31
3.3	Centrality Measurement	33
3.4	Simulation	35

3.4.1	Glauber Monte Carlo Simulation	35
3.4.2	Event Generator	36
3.4.3	GEANT Simulation	38
3.5	Measurement of Charged Particle Multiplicity	38
3.5.1	Pseudo-Rapidity Distribution	38
3.5.2	Total Multiplicity	39
4	Results and Discussions	45
4.1	Collision Centrality Scaling	45
4.2	Collision Energy Scaling	45
5	Conclusion	49

Chapter 1

Introduction

1.1 Quark Gluon Plasma

A recurring theme in the history of physics is the desire to study nuclear matter under extreme conditions. There is considerable interest in the fate of nuclear matter when subjected to density and temperature extremes [1, 2, 3]. According to Quantum ChromoDynamics (QCD) theory as the underlying theory of strong interaction, quarks and anti-quarks, which are elementary particles in the QCD frame, interact with one another exchanging gluons, namely strong force. In the normal condition, color-charged quarks are always confined in neutral color (color-singlet) states, comprising baryons (3-quark bound state) or mesons (2-quark bound state) by exchanging their color charges through gluons. Collins and Perry noted in 1975 [4] that the reduction of the coupling constant at small distances indicated that the dense nuclear matter at the center of neutron stars would consist of deconfined quarks and gluons. Their treatment focused on the high density, low temperature regime of QCD, but they did note that similar arguments might apply to the high temperatures present in the early universe. Just before the hadrons were formed, in a few μs after the big bang, the universe consisted of the melted soup of quarks and gluons. Under these extremely high density and/or temperature condition, the color force between quarks for long distance is screened by dense gluons, allowing quarks to propagate for a long distance. In such a medium, when the energy density ϵ exceeds some typical hadronic value ($\sim 1 GeV/fm^3$), matter no longer consists of separate hadrons (protons, neutrons, etc.), but as their fundamental constituents, quarks and

gluons. Because of the apparent analogy with similar phenomena in atomic physics, this phase of matter may be called the QCD (or quark gluon) plasma (QGP). At recent lattice QCD calculation [5] results in that the transition temperature at zero baryon density is 170MeV.

High energy nuclear collisions would provide the unique opportunity to study the nature of nuclear matter at such a high energy density, which could be the QGP state, in the laboratory. Figure 1.1 shows a phase diagram of nuclear matter as a function of baryon density and temperature, and how the QGP state can be explored in high energy nuclear collisions. To study nature of the state of high baryon and/or energy density, enormous experimental efforts have been carried out in the fixed target programs using Bevatron at Lawrence Berkeley National Laboratory (LBNL), the Alternating Gradient Synchrotron (AGS) at Brookhaven National Laboratory (BNL), and the Super Proton Synchrotron (SPS) at European Organization for Nuclear Research (CERN). Following the fixed target experiments till 1999, the study of high energy nuclear collisions has opened a new stage with the Relativistic Heavy Ion Collider (RHIC) at BNL, where the initial energy density in central collision is expected to be sufficient for QGP formation.

1.2 Particle Production

In the relativistic heavy ion collisions, nuclei are contracted in the beam direction like pancakes due to the Lorentz boost. Figure 1.2 shows a schematic drawing of a heavy ion collision. The number of nuclei participating in the collision, called "participants", and the rest that do not participate in the collision, called "spectators", could be geometrically determined by cut with the straight line at the impact parameter b , namely the length of the overlap region of colliding two nuclei.

The high multiplicities in heavy ion collision typically arise from the large number of nucleon-nucleon collisions which occur, since many of the nucleons strike several times as they pass through the oncoming nucleus. Thus, mechanism of particle production in heavy ion collision is complicated due to its large number of nucleon-nucleon collisions and nuclear effects which is occurred in high energy acceleration.

On the other hand, both e^+e^- collision and $pp/\bar{p}p$ collisions must ultimately allow a description based on QCD, the theory of the strong interaction. The large momentum transfer to the outgoing produced quark and anti-quark

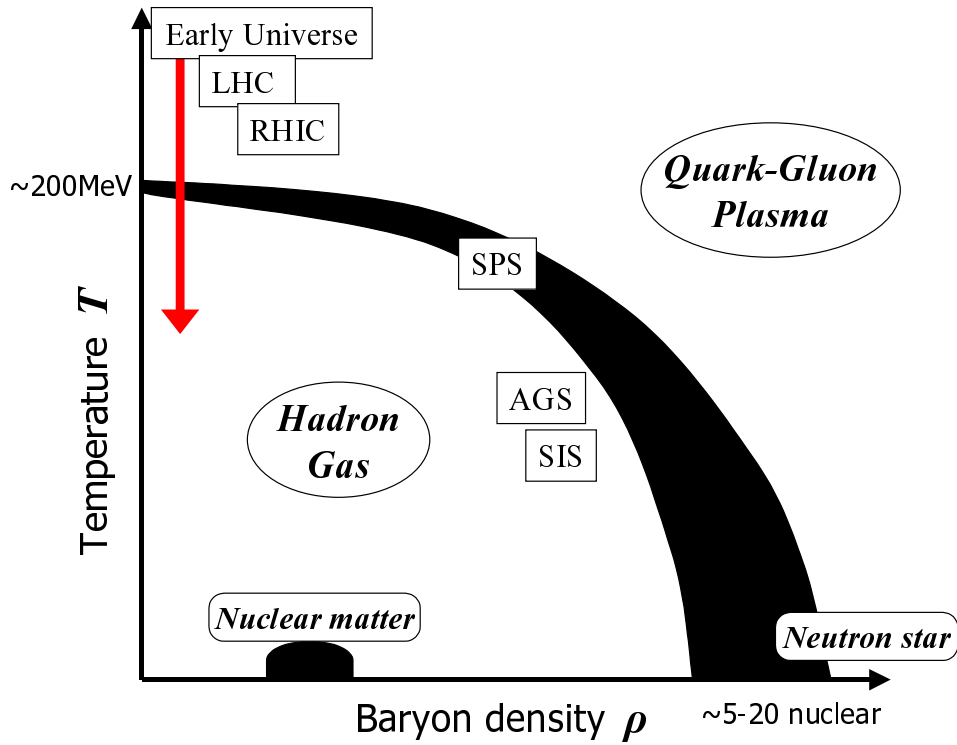


Figure 1.1: A phase diagram of nuclear matter as a function of baryon density ρ and temperature T . Hadronic phase is shown at low density and temperature, and the QGP phase is shown at high density and/or temperature, separated by mixed phase shown by the black band [13].

in e^+e^- reactions allows the use of perturbative QCD to describe the spectrum of quarks and gluons radiated as the system fragments [6]. $pp/\bar{p}p$ collisions are not generally thought to be amenable to such a perturbative description, since the transverse momentum exchanges involved are typically less than $1\text{GeV}/c$. Instead, phenomenological approaches (e.g. PYTHIA [7]) are used to describe the spectrum of particles. The crucial difference between e^+e^- collision and $pp/\bar{p}p$ collisions is existence of leading partons in pp collisions. Due to it, available center of mass energy for particle production is reduced in $pp/\bar{p}p$ collisions. However available multiplicity of primary charged particles ($\langle N_{ch} \rangle$) in pp collision is similar to that for e^+e^- collision with $\sqrt{s_{e^+e^-}} = \sqrt{s_{eff}}$, where $\sqrt{s_{eff}}$ is the pp center of mass energy minus the energy taken away by the leading parton. This is interpreted as a universal mechanism of particle production controlled dominantly by the available center of mass energy [8, 9].

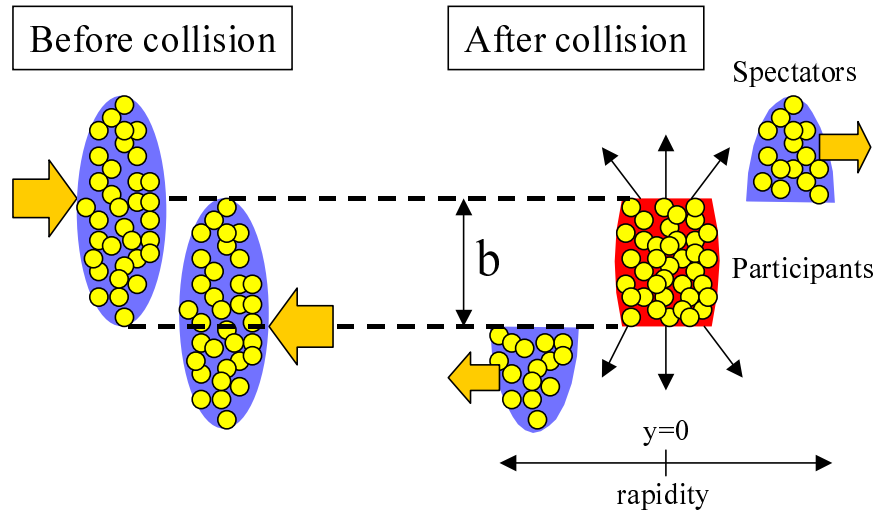


Figure 1.2: A schematic drawing of a heavy ion collision. Nuclei are geometrically separated into participants and spectators for the impact parameter b [13].

1.3 Motivation of This Study

Studies of hadron nucleus interaction demonstrated that the average multiplicity of primary charged particles ($\langle N_{ch} \rangle$) did not scale proportionally to the number of binary collisions (N_{coll}) in the reaction, but rather was found to scale with the number of wounded nuclei participating inelastically in the collision (N_{part}) [10, 11]. Thus, by scaling the particle yields measured in heavy ion collisions by $N_{part}/2$, the data from heavy ion collisions may be directly compared with similar yields in elementary pp , $\bar{p}p$, or even the annihilation of e^+e^- into hadrons. Comparisons with e^+e^- collision and $pp/\bar{p}p$ collisions are made to investigate whether confinement of quarks and gluons is broken in high energy heavy ion collisions or not. The naive view is that N_{ch} in heavy ion collision scales to the $pp/\bar{p}p$ collisions if there are not something special. However, if it scales to e^+e^- collision, then, it may be quite remarkable issue. In this paper, I report the results of the measurement of multiplicity of primary charged particles per pseudo-rapidity ($dN_{ch}/d\eta$) and N_{ch} as a function of collision centrality for high energy Au+Au collisions at $\sqrt{s_{NN}} = 200\text{GeV}$, where $\sqrt{s_{NN}}$ is the center of mass collision energy per nucleon pair.

In Chapter 2, the accelerator facilities and experimental setup of detectors are introduced. In particular, subsystem, which is utilized to detect charged particles in forward rapidity region, is explained in detail.

In Chapter 3, the method for calibration for subsystem, simulation tools, and measurement of $dN_{ch}/d\eta$ especially in forward rapidity region, are introduced. For central rapidity region ($|\eta| < 0.35$), $dN_{ch}/d\eta$ has been already measured by using the central detectors in PHENIX [12]. Thus, in this paper, I focus to the measurement for forward rapidity region.

In Chapter 4, the results of my analysis are reported. Then the N_{ch} which is obtained in Au+Au collisions is discussed by comparison with e^+e^- collision and $pp/\bar{p}p$ collisions, where N_{ch} is scaled by $N_{part}/2$.

Finally, I give the conclusion of this analysis in Chapter 5.

Chapter 2

Experimental Setup

2.1 Relativistic Heavy Ion Collider

The Relativistic Heavy Ion Collider (RHIC) at Brookhaven National Laboratory (BNL) has a capability to accelerate and collide several types of particle species, e.g. gold-gold (Au+Au), deuteron-gold (d+Au) and polarized proton-proton (p+p) collisions. A schematic diagram of the RHIC facility is shown in Figure 2.1. In Au+Au collisions, bunches of Au ions are provided from the Tandem-Van-de-Graaff and accelerated up to 1A MeV, then injected into the Booster Synchrotron to accelerate up to 192A MeV, and then injected in the Alternating Gradient Synchrotron (AGS) ring. The AGS accelerator, which has been used for many fixed target experiments in heavy ion collisions at the center of mass energies from 2.5 to 4.5GeV, is used as a pre-accelerator for the RHIC ring. The bunches of Au ions, accelerated up to 10.8GeV by the AGS ring, are send to the AGS-To-RHIC transfer line, where a switching magnet sends the ion bunches down one of two beam lines. The two Au beams are injected into the right and left rings of RHIC, labeled yellow and blue ring, respectively. The injected two Au beams are accelerated up to 100GeV per nucleon in the RHIC ring, and collide at six beam interaction points. RHIC has the total length of 3.8km ring and number of bunches per ring is 60 and each bunch consists of $\sim 1 \times 10^9$ Au ions. In Au+Au collisions at $\sqrt{s_{NN}} = 200\text{GeV}$, designed luminosity is $2 \times 10^{26}\text{cm}^{-2}\text{s}^{-1}$. Four experiments are located at four of the six interaction points, i.e. PHENIX, STAR, PHOBOS and BRAHMS as shown by Figure 2.1.

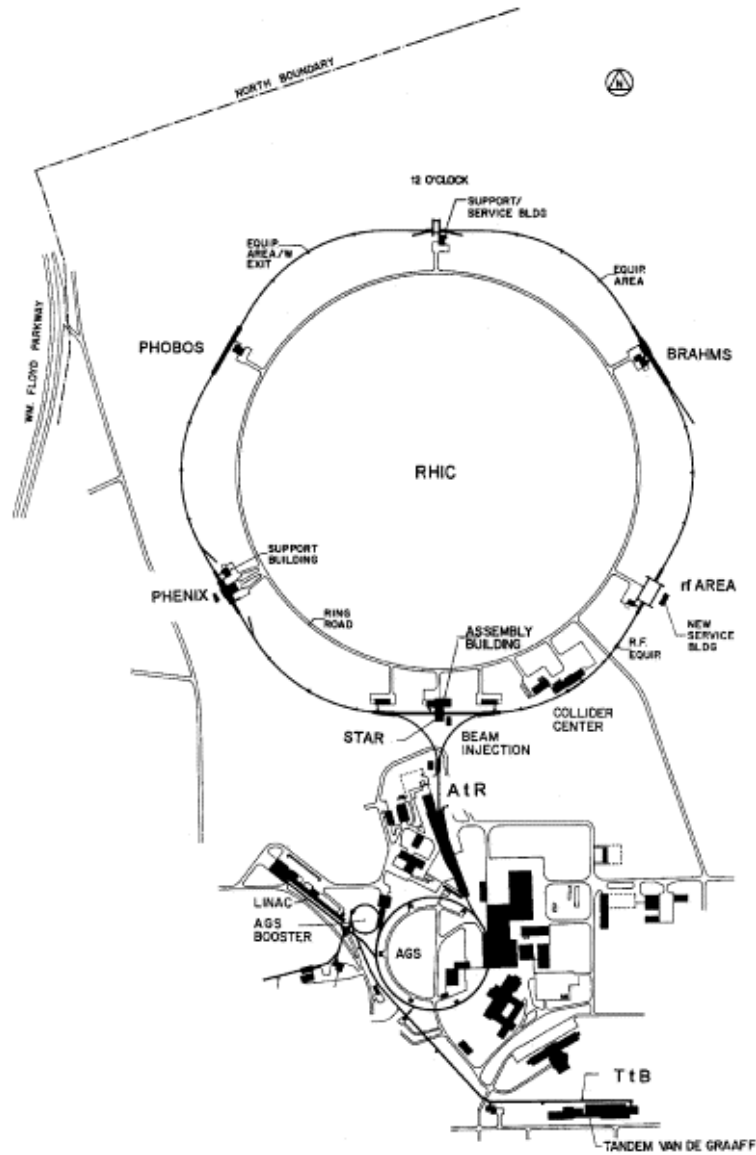


Figure 2.1: A schematic diagram of the AGS and RHIC facilities [13].

2.2 PHENIX Detector

The Pioneering High Energy Nuclear Interaction eXperiment (PHENIX) is an exploratory experiment for the investigation of high energy collisions of heavy ions. The purpose of the PHENIX is to provide powerful particle identification capabilities for hadrons, leptons, and photons over a wide momentum range. The PHENIX consists of a collection of detectors, each which perform a specific role in the measurement of the results of a heavy ion collision. The detectors are grouped into two central arms, which have pseudo-rapidity coverage of $|\eta| < 0.35$ and 90 degree azimuthal angle for each arm and are capable of measuring a variety of particles, and two muon arms which have pseudo-rapidity coverage of $1.2 < |\eta| < 2.4$ and focus on the measurement of muon particles. There are also additional event characterization detectors that are specialized to make triggers and to measure the luminosity and the centrality in heavy ion collisions, and a set of three huge magnets that bend the trajectories of the charged particles. Figure 2.2 shows the bird view of PHENIX detector. And detector setup for second year is shown in Figure 2.3 .

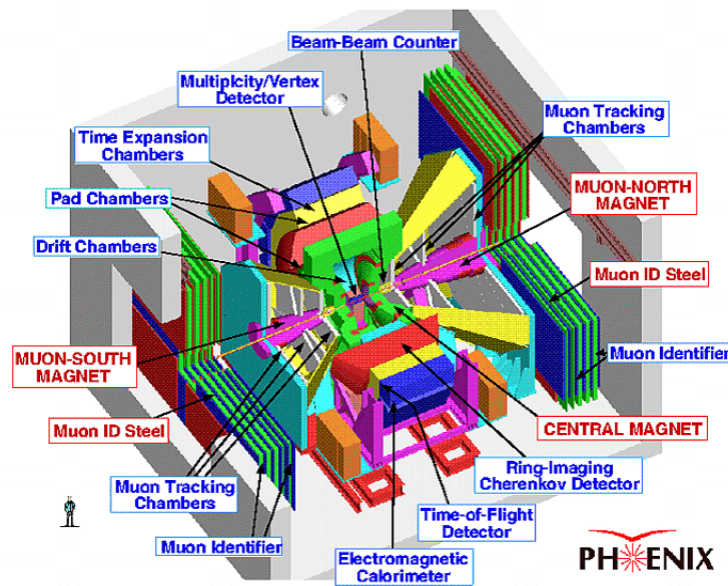


Figure 2.2: Overview of PHENIX detectors [14].

PHENIX Detector - Second Year Physics Run

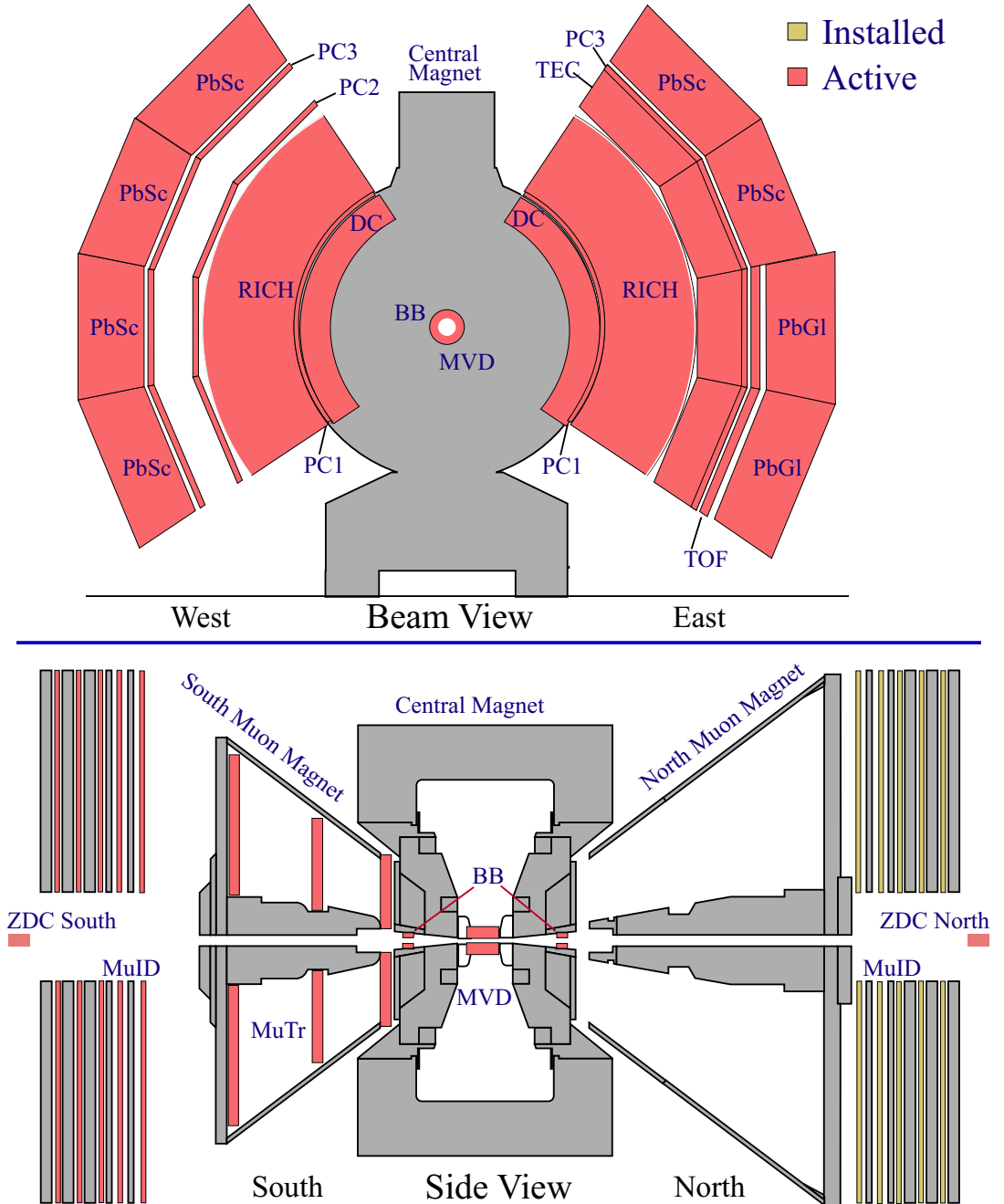


Figure 2.3: Schematic drawings of the PHENIX detector setup for second year running, viewed in a cut through the collision vertex (top figure), parallel to the beam axis (bottom figure) [15].

2.2.1 Magnet

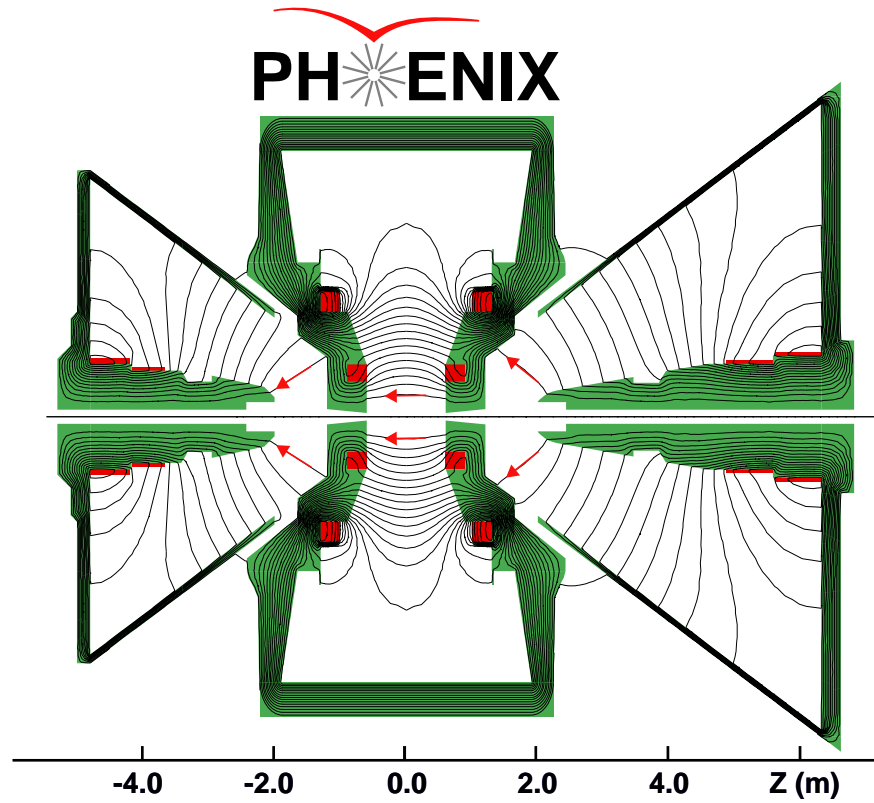
The central magnet (CM) consists of inner coil, outer coil and return yoke. They provide cylindrical magnetic field optimized to the different physics programs for central arms because of the two independent coils. The Muon Magnet (MM) uses two solenoidal coils to produce a radial magnetic field. The coils are wound around a tapered piston and the flux propagates out to the lampshade. Figure 2.4 illustrates a vertical cutaway view of the PHENIX magnets with the magnetic field lines. Due to the magnetic field, the charged particles with the momentum of less than 0.2GeV/c are trapped in the field. During the run for this work, both coils are not activated because multiplicity of charged particles is measured in this paper and I do not need to know the momentum information in this case.

2.2.2 Beam Beam Counter

The Beam Beam Counters (BBC) are placed at 144.35cm along to beam pipe from the nominal collision vertex point and covers the pseudo-rapidity of $3 < |\eta| < 4$ and 2π in azimuthal angle surround the beam pipe (see Figure 2.2). Each of BBC consists of 64 Cerenkov counters, each of which consists of a quartz Cerenkov radiator and a mesh-dynode photo multiplier tube (PMT) readout. Since the magnetic field around BBC is expected to be about 3kG, these PMTs are designed to work in such a high magnetic field environment. Quartz has the 3cm thickness and refractive index of 1.47. Therefore, the BBC detects charged particles, of which beta is more than 0.68. Figure 2.5 shows the one side of BBC and the one of elements of BBC is shown in Figure 2.6. The BBC is designed to measure the number of charged particles produced by the collisions and to measure the collision vertex, collision time and collision centrality. Collision timing is evaluated from the average of the arrival times as:

$$t_{T0} = \frac{(T_1 + T_2 - \frac{2L}{c})}{2} \quad (2.1)$$

where T1 and T2 are the observed values of arrival time at each side and L is the length from the collision point to the surface of BBC. The c is velocity of light. Collision vertex is evaluated from the difference of the arrival times



Magnetic field lines for the two Central Magnet coils in combined (++) mode

Figure 2.4: A simulation of the magnetic field lines inside the three PHENIX magnets. The arrows on the inner field lines represent the field direction [15].

as:

$$Z_{vertex} = \frac{(T_1 - T_2) \times c}{2} \quad (2.2)$$

The collision timing is served as a start time for the time of flight measurement. The time resolution of each BBC is evaluated to be around $524ps$. The vertex position accuracy is estimated to be better than 1 cm.



Figure 2.5: A picture of BBC array comprising 64 BBC elements [16].

2.2.3 Zero Degree Calorimeters

The Zero Degree Calorimeters (ZDC) is placed at 18.25m along to beam pipe from the nominal collision vertex point (see Figure 2.2). Each of them consists of alternating tiles of plates of tungsten and layers of optical fibers. The direction of the plates and layers are tilted by 45 degree relative to the incident neutron direction to collect the Cerenkov light as shown in Figure 2.7. The ZDC are designed to measure spectator neutron which do not participate in the collision and to determine the collision vertex and collision centrality. Thus both north and south ZDC sit at just upstream of the last bending magnet on the RHIC ring which is shown by Figure 2.8.

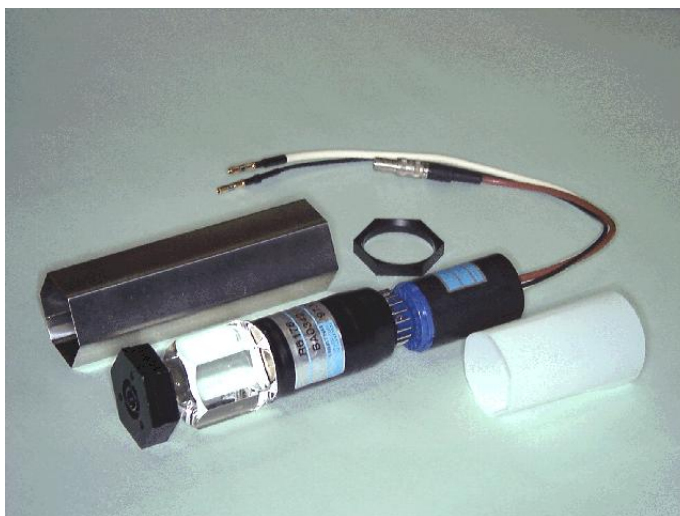


Figure 2.6: A picture of elements of BBC, which is consists of quartz and PMT [16].

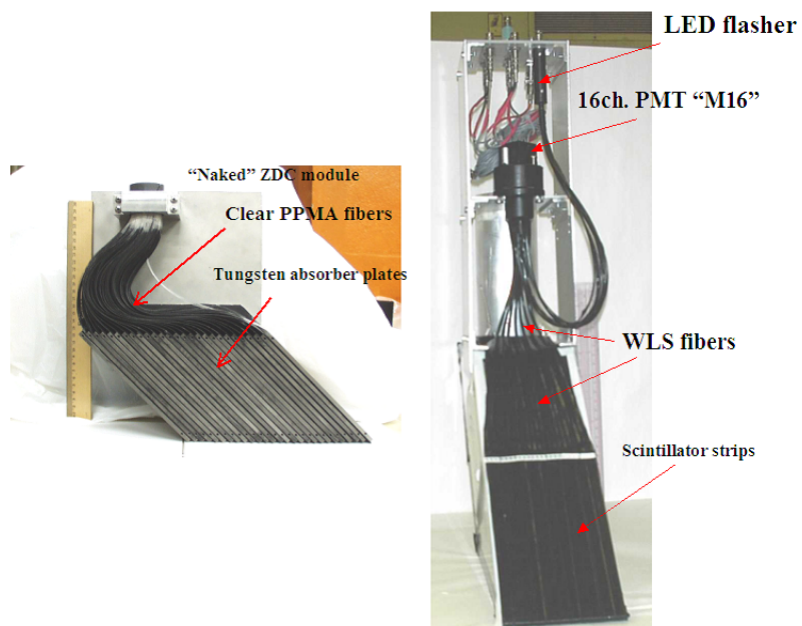


Figure 2.7: A picture of ZDC of one side [17].

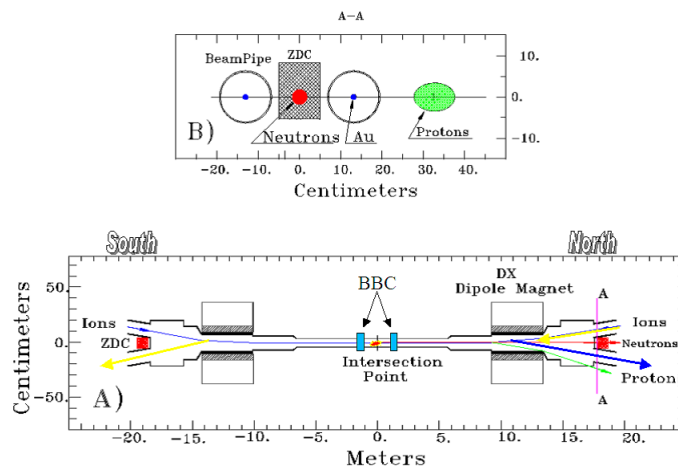


Figure 2.8: A schematic drawings of ZDC. Bottom figure shows a top view of the beam geometry and ZDC location. Top figure shows a beam's eye view of the ZDC location [17].

2.2.4 Drift Chamber

The Drift Chamber (DC) is placed between 2.02m and 2.46m in the radial distance from the nominal interaction point and consists of 3 different direction of the wire: same directions as the beam pipe which is namely X module, and ± 6 degree tiled angled relative to the beam pipe direction. The detector consists of 2 modules for each direction which are namely U and V module, respectively. Difference in the design of X and U, V module is conditioned by the fact that X module should provide wire to run along z axis. On the contrary, U, V module should provide some slope of wires with respect to z axis. A module consists of 4 or 12 anode wires depending on the wire direction. In total, 40 drift cells are located in different radii. Each sector is filled with 50-50% Argon-Ethane gas mixture. The designed position resolution in a single wire is 0.15mm and the two track resolution is 1.5mm.

2.2.5 Pad Chamber

The Pad Chamber (PC) consists of 3 layers; PC1 at 2.5m, PC2 at 4.1m and PC3 at 5.0m apart from the beam pipe and each layer consists of 8 sectors. The PC is designed as a multi wire proportional chamber with readout of the

cathode pads. Each pad has either $8.2 \times 1.5 \text{mm}^2$ or $8.2 \times 2.7 \text{mm}^2$ dimension. A single pixel is small copper rectangle which is connected to 8 other small copper rectangles. All 9 pixels are read out by a single discriminator. The object which is composed of 9 connected pixels is called a "pad". Whenever a charged track passes through the pad chamber, there should be three neighboring pads which all receive an induced signal large enough to trigger their three separate discriminators. The 9 fold ambiguity of which pixel is hit is resolved by looking at which set of three pads has hits. The structure of three neighboring pixels which gets uniquely identified as the location of the track is called a "cell". The designed position resolution for the cell is $\pm 4 \text{mm}$. The purpose of the detector is to measure the charged multiplicity and to reduce the background in the sample of charged particles.

2.2.6 Ring Imaging Cerenkov Hodoscope

The Ring Imaging Cerenkov Hodoscope (RICH) is designed to identify the electron, positron and high p_T charged particle. Each of the detectors in the east and west arms has a volume of roughly 40m^3 and minimum thickness of 87cm of the gas at atmosphere pressure, which is CO_2 gas is used. The Cerenkov photons produced in the gas are reflected on the mirror and are detected by the PMT. The average radius of Cerenkov ring is 8cm and the average number of the Cerenkov photons produced by electron is 11 on the plane where the PMT are sitting.

2.2.7 Time Expansion Chamber

The Time Expansion Chamber (TEC) is sitting only in the east arm at the distance between 4.2 and 4.9m apart from the beam pipe. It consists of 6 cells with 3cm drift length in different radii. The drift time, position and the pulse height are measured by the anode wires. This detector is designed to improve the momentum resolution at the higher p_T than 4GeV/c and to identify electron and positron using the energy loss information.

2.2.8 Time of Flight

The Time Of Flight detector (TOF) consists of 960 scintillator slats which has 1.5cm width and 1.5cm length. It covers 45 degree in the azimuthal

angle. The designed time resolution is 100 ps . the TOF has capability to identify the charged pion and kaon at p_T up to 2.5GeV/c.

2.2.9 Electro Magnetic Calorimeters

The Electro Magnetic Calorimeters (EMCal) is the primary tool for measuring photons. There are two kind of calorimeter in the PHENIX. One is a shashlik type lead scintillator sampling calorimeter (PbSc) and another is a lead glass calorimeter (PbGl). The PbSc sectors fully cover the acceptance of the west arm, half cover the which of the east arm and each of them consists of 18 (3×6) super modules. Each of super module consists of 36 (6×6) modules. Each of module consists of 4 (2×2) towers. Then, each of towers consists of sampling cells made of alternating 65 lead tiles and 66 scintillators tiles whose thickness are 4.0mm and 1.5mm, respectively. Therefore, Each sector consists of 2592 (36×72) individual towers. The surface area of each tower is $5.52 \times 5.52cm^2$ and the active depth is 37.5cm with 18 radiation lengths. The sampling cells are optically connected by 32 longitudinally penetrating wavelength shifting fibers and collected light signals are read out by a PMT at the back of the tower. The PbGl is a Cerenkov type calorimeter. A lead glass has 4.0×4.0 cross section and 40cm length. The entire array comprises 9216 tower previously, which are individually wrapped with aluminized mylar foil and shrink tube and are isolated optically.

2.2.10 Muon Spectrometers

The muon spectrometers are located at the pseudo-rapidity ranges of $-2.25 < \eta < -1.15$ (the south muon arm) and $1.15 < \eta < 2.44$ (the north muon arm) with the full azimuthal coverage. Each muon arm is composed of the Muon Tracker (MuTr) with the Muon Magnet and the Muon Identifier (MuID). It is designed to measure vector mesons. Each MuTr provides trajectories of charged particles and is composed of three stations of cathode-strip readout tracking chambers. The MuID is comprised of six walls of steel absorbers interleaved with five layers of plastic proportional Iarocci tubes.

2.3 Trigger and Data Acquisition system

The PHENIX detector consists of several subsystems and each has hundreds to thousands readout channels. The interaction rate at designed luminosity is a few kHz for Au+Au central collisions. To handle a high rate and a large amount of data, the PHENIX Data Acquisition (DAQ) system is designed by using the pipeline processing technique which is performed by simultaneous triggering and readout as shown in Figure 2.9. This is accomplished through the features of detector front ends and the ability to accommodate higher level triggers. In order to preserve the high interaction rate capability, a flexible triggering system that permits tagging of events is constructed. The PHENIX DAQ system has two types of triggering levels, denoted as level 1 (LVL1) and level 2 (LVL2). The LVL1 trigger system is composed of the Local Level 1 (LL1) systems which communicate with some participant detectors, and the Global Level 1 (GL1) system which provides a trigger decision according to the LL1 algorithm.

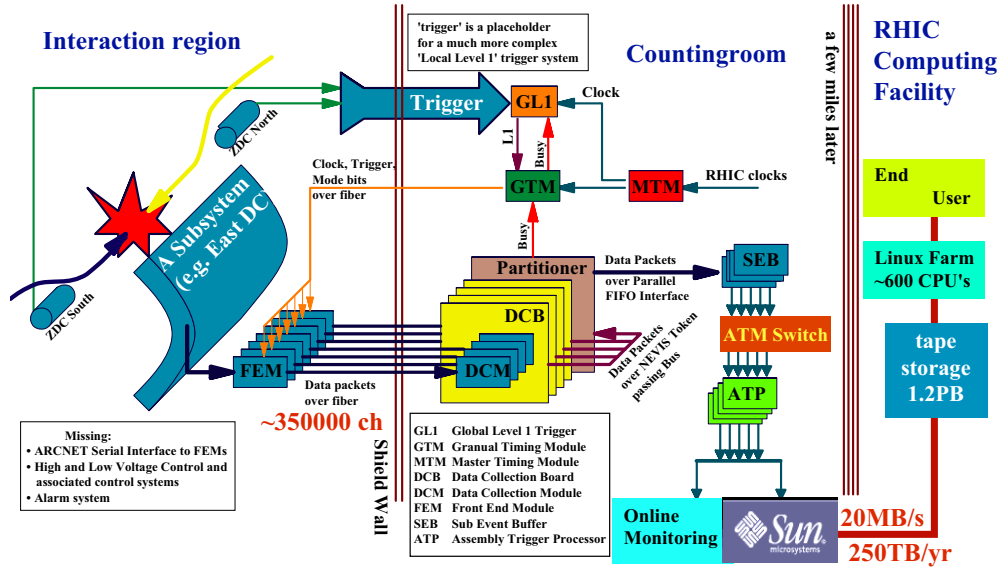


Figure 2.9: Illustrates the block diagram of the DAQ system in detail. Signals from the various PHENIX subsystems are processed by Front End Module (FEM) that convert the analog signals into digital signals. If the LVL1 trigger accepts a collision event, the LVL1 trigger sends a signal to the Granular Timing Module (GTM) in conjunction with the RHIC clock provided by the Master Timing Module (MTM). The GTM requires the FEM to send its digitized data to the Data Correction Module (DCM). Many parallel data stream from the DCM are sent to the Event Builder (EvB). The EvB performs the final stage of event assembly, which is named as PHENIX Raw Data File (PRDF), and provides an environment for the LVL2 trigger [15].

Chapter 3

Data Analysis

3.1 Run Summary and Trigger Selection

In the Year 2 Au+Au running at RHIC (2001~2002), the PHENIX took the minimum bias events which have been taken by the LVL1 trigger determined by the two LL1 trigger requirements for BBC and ZDC as:

- At least two PMT are fired in each BBC (north side and south side, respectively). And the collision vertex measured by BBC is within 75cm.
- At least one forward neutron has to be registered in each ZDC.

The minimum bias events include collision events from central to peripheral in 92% of the interaction cross section and. The LVL2 trigger is used to take only interesting physics events. The PHENIX accumulated the integrated luminosity $\int Ldt \sim 24mb^{-1}$. Figure 3.1 shows a summary plot of luminosity measured by 4 experiments at RHIC.

3.2 Calibration

In this section, the calibration method for PMT which is component of BBC, and Front End Modules (FEM) read out modules. PMT calibration is based on event data in Au+Au collisions, on the other hand, FEM calibration is based on special data taken by using internal test pulse or external injected pulse.

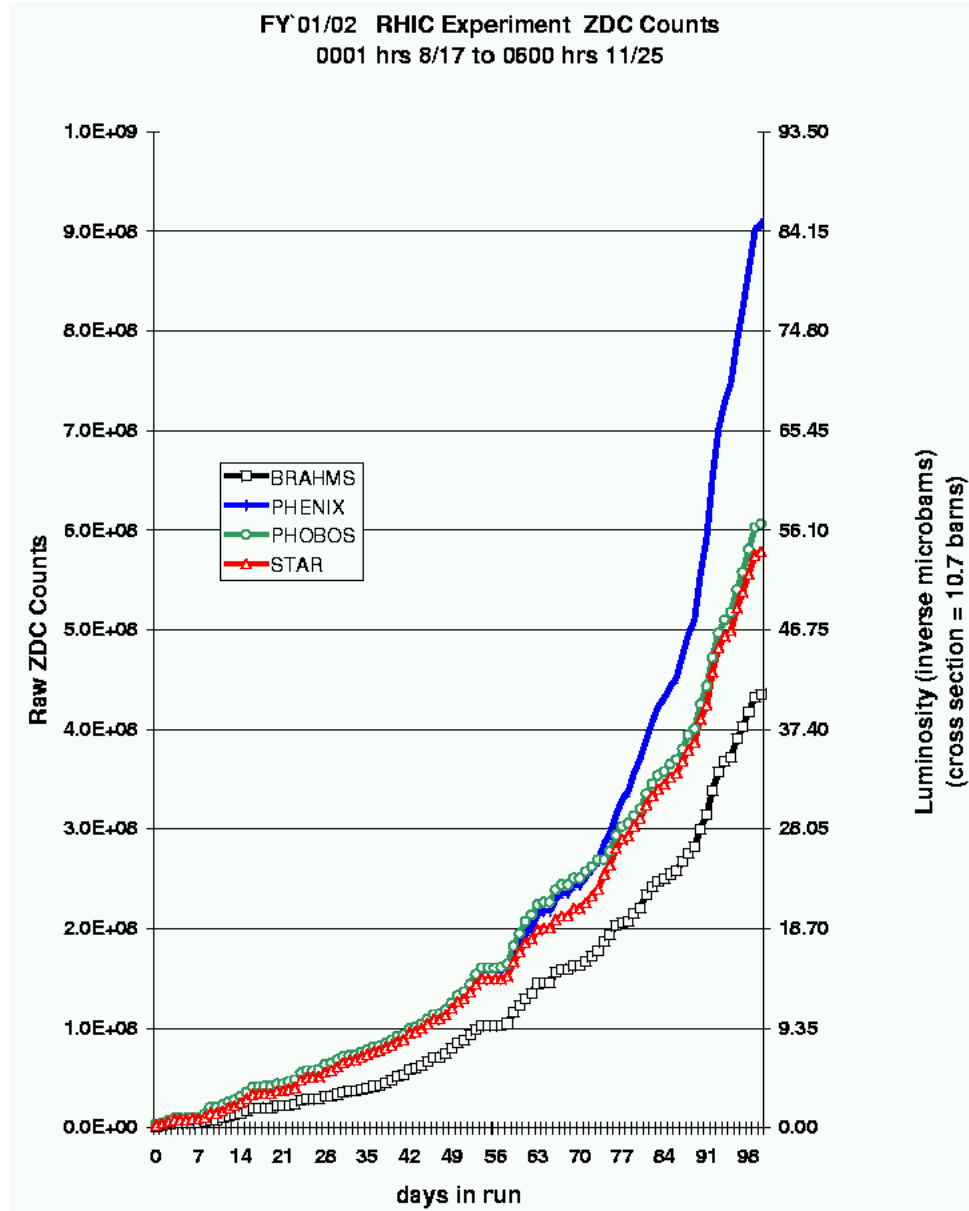


Figure 3.1: Luminosities estimated by PHENIX (blue), STAR (red), PHOBOS (green) and BRAHMS (black) for Year2 Au+Au running [15].

3.2.1 FEM Calibration

Pedestal measurement: Usually pedestal values can be measured as Analog to Digital Converter (ADC) channels when zero charge is injected. But this general method cannot be used, because our ADC is self gated ADC, that is, the ADC gate does not open until the injected charge exceed a certain threshold. Thus pedestal values can be measured based on scanned data by changing Digital to Analog Converter (DAC) values. After slope between DAC values and ADC values is obtained, the pedestal values are determined by extrapolating the slope at the zero DAC values as shown in Figure 3.2.

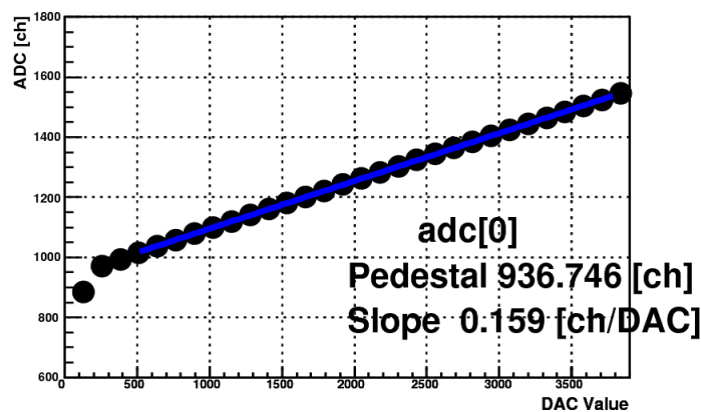


Figure 3.2: Measured ADC channels as a function of DAC value. Pedestal was obtained by extrapolating the fit line at the zero DAC value.

ADC conversion factor measurement: Conversion factors from ADC values to charge values of PMT output are estimated by external charge injections. The external charge is created by function generator and that values are determined by charge integrated by using digital oscilloscope. After slope between injected charge value and ADC value is obtained, conversion factors are determined by slope parameters of linear function fit as shown in Figure 3.3.

TDC conversion factor measurement: Conversion factor from TDC values to time values can be measured based on scanned data by changing delay setting for the test pulse injection. In the case of PHENIX DAQ system, the timing of stop pulse injection is fixed relative to GTM. The delay values indicate the time between GTM timing and start timing pulse injection.

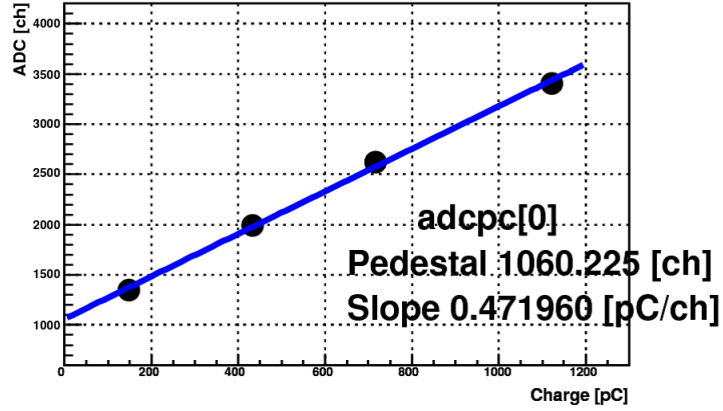


Figure 3.3: Measured ADC channels as a function of injected charge. Conversion factors were determined by inverse slope parameter fit with linear function.

When the delay values increase, TDC values decrease. After slope between TDC values and delay values is obtained, conversion factors are determined by slope parameter of linear function fit as shown in Figure 3.4.

TDC overflow measurement: The overflow values in TDC channel are important parameters, since they define whether hit are valid or not. When stop timing is not injected until TDC gate is closed, the overflow values are output. Typical overflow distribution is Gaussian so that the distribution is fit by its function. The overflow values are determined by mean and sigma of function as shown in Figure 3.5.

3.2.2 Gain Calibration

Determination of operational high voltage: Expected PMT gains are estimated based on values of ADC channel which are obtained when one charged particle is injected to BBC, denoted by "MIP", together with gain curve of each PMT obtained by laser pulse injection. The gain curve will be fit with an empirical function;

$$f(HV) = \exp(p_0 + p_1 \times HV + p_2 \times HV^2) \quad (3.1)$$

where p_0 , p_1 , and p_2 are parameters. In order to get absolute scale which provides us optimal operational high voltage values, the gain curve is scaled

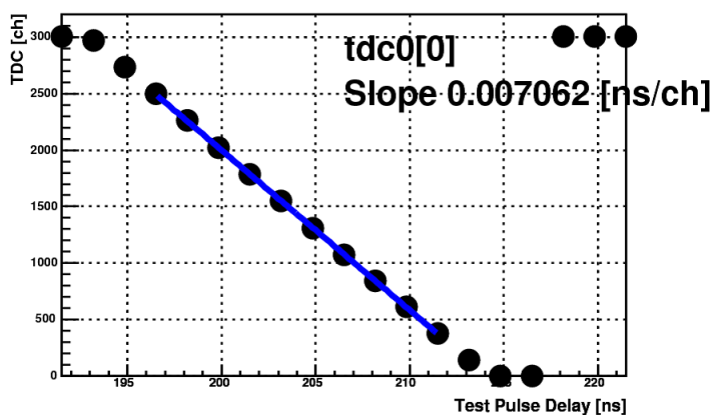


Figure 3.4: Measured TDC channels as a function of delay setting of test pulses. Conversion factors were determined by inverse slope parameter fit with linear function.

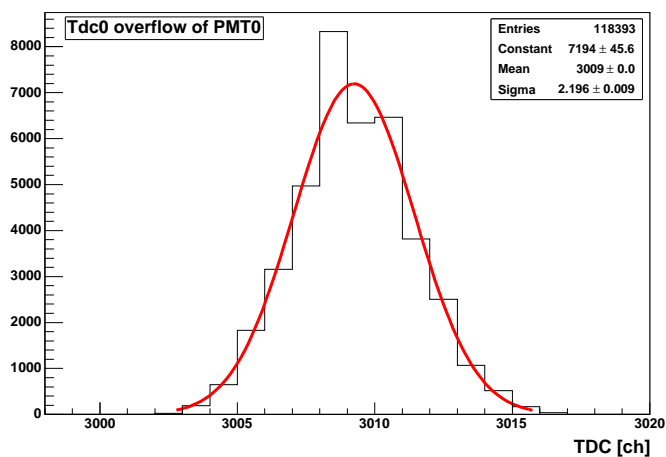


Figure 3.5: TDC overflow distribution as a function of TDC channel. Fitted Gaussian is shown by red line on the distribution and parameters of result of fit are shown in the right box on the figure.

with MIP values. Based on the curve, the operational voltage values which would produce 40pC for one MIP are determined. Once operational values are obtained for each PMT, we take an average high voltage values over typically eight PMTs in a HV group. Figure 3.6 shows the result of determination of HV.

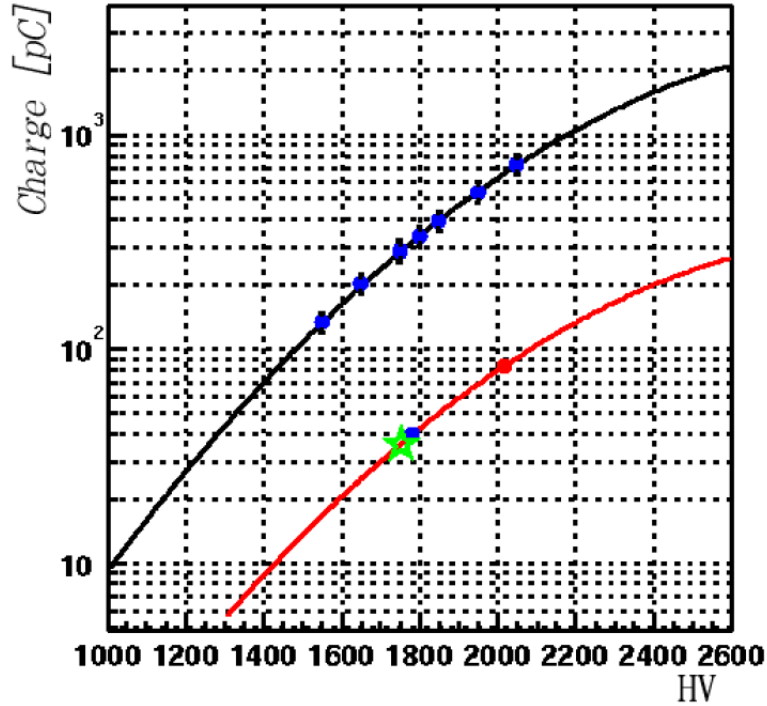


Figure 3.6: The gain curve of a PMT by laser (black line). Data points of laser peak with different HV values are shown as blue points on the black line. Red line shows the scaled gain curve to the MIP peak at the pre-condition of HV setting, which is indicated as red point on the red line. Blue point on the red line is the target HV values for each PMT, which is set by 40pC for output charge of PMT. The operational voltage of each PMT is shown as green star, which is calculated by the average values of belonging HV group [18].

PMT gain measurement: PMT gains are estimated based on one MIP values. In order to select one MIP event, certain condition is attached, which is a constraint of no hit in surround the certain PMT. MIP peak will

be clarified so that ADC distribution is fit by empirical function as shown in Figure 3.7;

$$f(ADC) = \frac{2 \times \exp(p_0 + p_1 \times ADC + \frac{p_2}{ADC})}{1 + \exp(\exp(-\frac{ADC-p_3}{3}))} + p_4 \times \exp(-\frac{(ADC - p_5)^2}{2 \times p_6^2}) \quad (3.2)$$

where from p_0 to p_6 are parameters. ADC distribution can be separated to MIP distribution and background distribution. Background distribution is estimated by empirical function;

$$f(ADC) = \frac{2 \times \exp(p_0 + p_1 \times ADC + \frac{p_2}{ADC})}{1 + \exp(\exp(-\frac{ADC-p_3}{3}))} \quad (3.3)$$

and MIP distribution is declared by Gaussian function. After fitting to ADC distribution, background is subtracted with background function. Then MIP values are estimated by Gaussian function fit to MIP distribution which is ADC distribution after the background distribution is subtracted as shown in Figure 3.8.

3.2.3 Time Calibration

The slewing effect represents the timing difference as the signal height output from PMT, traverses the threshold values of discriminator in FEM which defines whether it is hit event or not. If pulse height is large, slewing effect is small. On the other hand, if pulse height is small, slewing effect becomes significant. In order to correct the slewing effect, new parameterization of slewing correction is implemented. At first, reference hit time in each side is calculated by taking an average of non slewing corrected hit time of PMT with valid hit. Its valid hit is defined by that TDC values are less than its overflow minus its sigma of overflow times four. Given a reference hit time per event, the time difference between the reference hit time and hit time of each PMT is measured. The time difference is plotted with respect to measured charge for each. This is named by slewing curve. Once the slewing curve is obtained, the curve is fit with the empirical function;

$$f(ADC) = p_0 + \frac{p_1}{ADC} + p_2 \times \log(ADC) + \frac{p_3}{ADC^2} \quad (3.4)$$

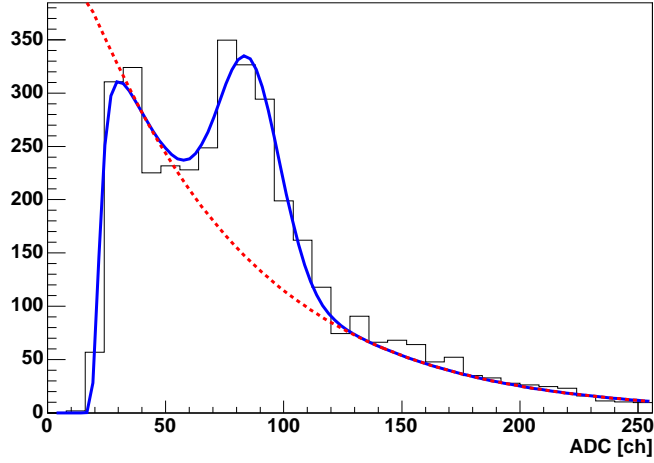


Figure 3.7: ADC distribution subtracted threshold values. Blue line shows fitted function of background plus MIP distribution which is Gaussian. Red line shows background function.

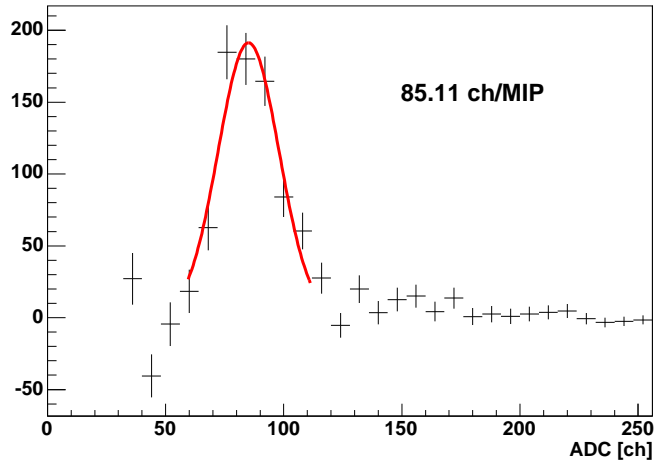


Figure 3.8: ADC distribution subtracted background. Red line shows Gaussian fit. PMT gain is determined by mean values of fit parameter divided by ADC gain constants.

where p_0 , p_1 , p_2 , and p_3 is parameters. Given slewing corrected hit time for each PMT, reference hit time is recalculated by using corrected hit time. The time difference between corrected reference hit time and non corrected hit time of each PMT is also measured. This iteration is repeated five times, since it is necessary to improve time resolution as shown in Figure 3.9. Finally, corrected reference hit time in each side is named by "arm hit time" and this is used for calculation of collision vertex and collision time. Figure 3.10 shows the corrected slewing curve using fitted function and Figure 3.11 shows the projectile of corrected slewing curve along the x axis.

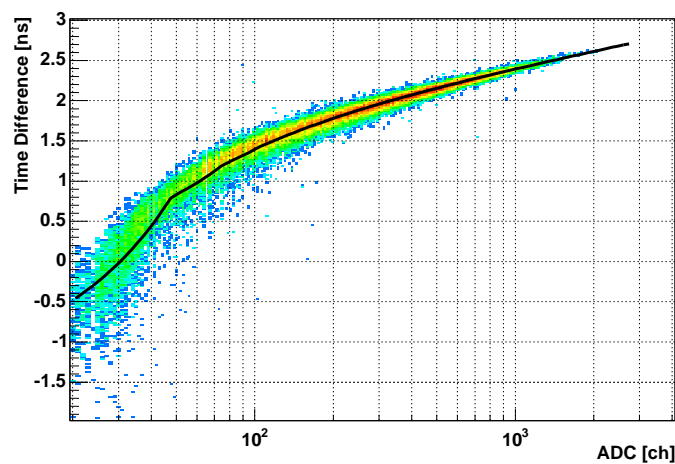


Figure 3.9: Typical slewing curve overlaid with fit slewing function.

3.3 Centrality Measurement

Collision centrality is the value which is related to impact parameter. Zero percentile of centrality indicates the collision between the two nuclei occurred with having zero impact parameter. When they collide with non zero impact parameter, charged particles emitted from interactive region are detected by BBC and spectator neutrons which is not participating with interaction are detected by ZDC. Schematic scenario is shown by Figure 3.12. After the boomerang plot of BBC versus ZDC is obtained, centrality is estimated by what is called by "clock method". The angle ϕ of a given event in the BBC

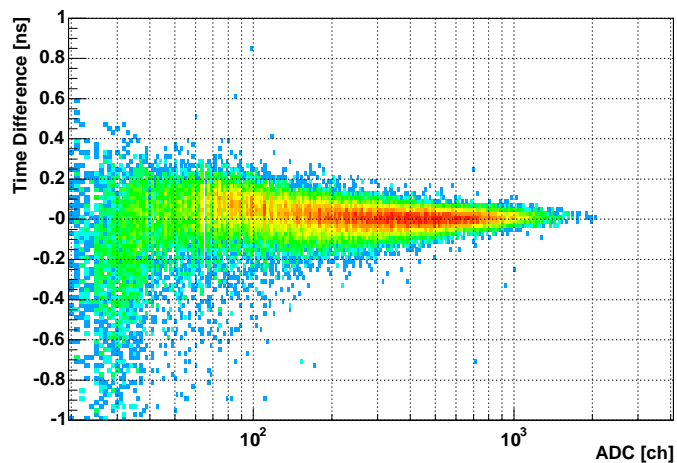


Figure 3.10: Corrected slewing curve.

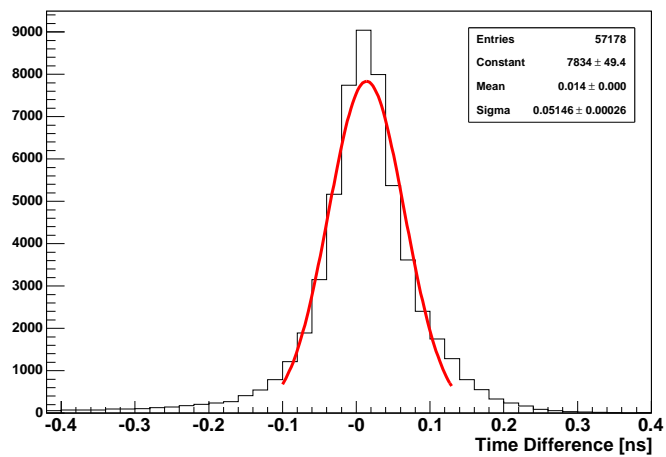


Figure 3.11: The timing difference between reference time and corrected timing of a PMT. The sigma of fit function is defined as the timing resolution.

ZDC plane is calculated with respect to the point $(0.2 \times BBC/BBC_{max}, 0)$ in the BBC ZDC plane. From Monte Carlo simulation (MC simulation) result, the angle ϕ is converted to percentiles of centrality.

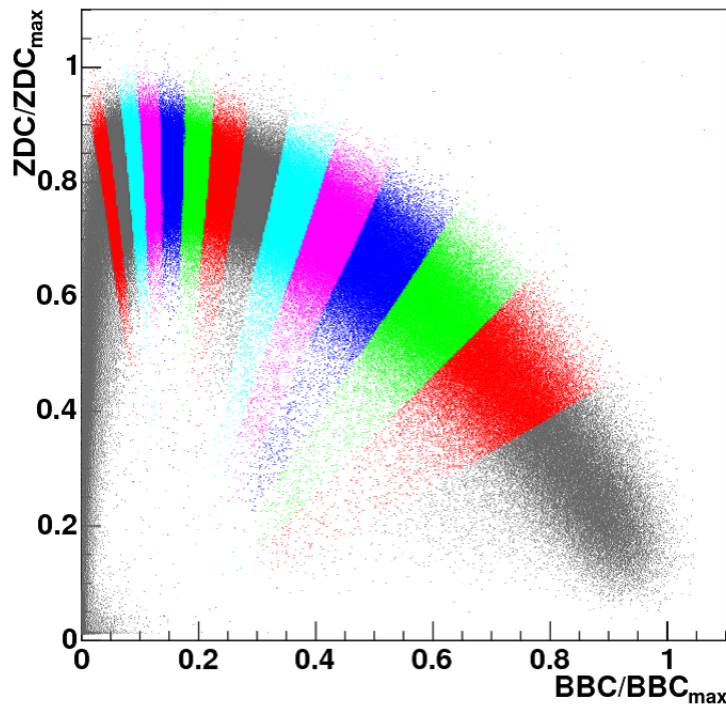


Figure 3.12: Scatter plot between BBC charge sum and ZDC energy sum. Color coding shows centrality class in 5 percent. BBC and ZDC is normalized by maximum values, respectively.

3.4 Simulation

3.4.1 Glauber Monte Carlo Simulation

The Glauber model is based on a simple geometrical picture of a nucleus-nucleus collision. Nucleons are assumed to travel on straight line trajectories, independent of whether they collide with other nucleons or not. After a nucleon is struck by another nucleon, one definitely has a highly excited

baryonic object. It is assumed in the Glauber model that the cross section for the interaction of this excited object with other ground state or excited nucleons is identical to the ordinary inelastic nucleon-nucleon cross section σ_{NN} . In the MC framework, the nucleons of the two Au nuclei are distributed in space according to the nucleon density profile. Then an impact parameter of the nucleus-nucleus collision is chosen randomly. A participant is defined as a nucleon that has suffered at least one inelastic nucleon-nucleon collision. The number of participants N_{part} is frequently used to characterize the centrality of a nucleus-nucleus collision, especially when reactions of nuclei with different mass number A are compared. Another quantity that can be calculated in the Glauber model is the average impact parameter $\langle b \rangle$ of a centrality class. The coordinate system is chosen such that the centers of the two nuclei are at $(-b/2, 0)$ and $(b/2, 0)$, respectively, where b denotes the impact parameter as shown in Figure 3.13. The nuclear density profile is parameterized by a Woods-Saxon function;

$$\rho(r) = \rho_0 \cdot \frac{1}{1 + \exp(\frac{r-R}{a})} \quad (3.5)$$

For gold nuclei the parameters

$$R = 6.38 fm \quad \text{and} \quad a = 0.54 fm \quad (3.6)$$

are used. For a center of mass energy of $\sqrt{s_{NN}} = 200 GeV$ an inelastic nucleon-nucleon cross section of $\sigma_{NN} = 42 mb$ was used in the Glauber calculations.

3.4.2 Event Generator

Heavy Ion Jet Interaction Generator (HIJING) Monte Carlo model is used in order to simulate the primary multiplicity in Au collision. HIJING basically is designed to simulate multiple jets and particle production in Au collision. PYTHIA subroutines and Lund jet fragmentation scheme are used. Detailed systematic comparison of HIJING results with a very wide range of data demonstrates that a quantitative understanding of the interplay between soft string dynamics and hard QCD interaction has been achieved. In particular, HIJING reproduces many inclusive spectra and two particle correlations, and explains the observed flavor and multiplicity dependence of the average transverse momentum.

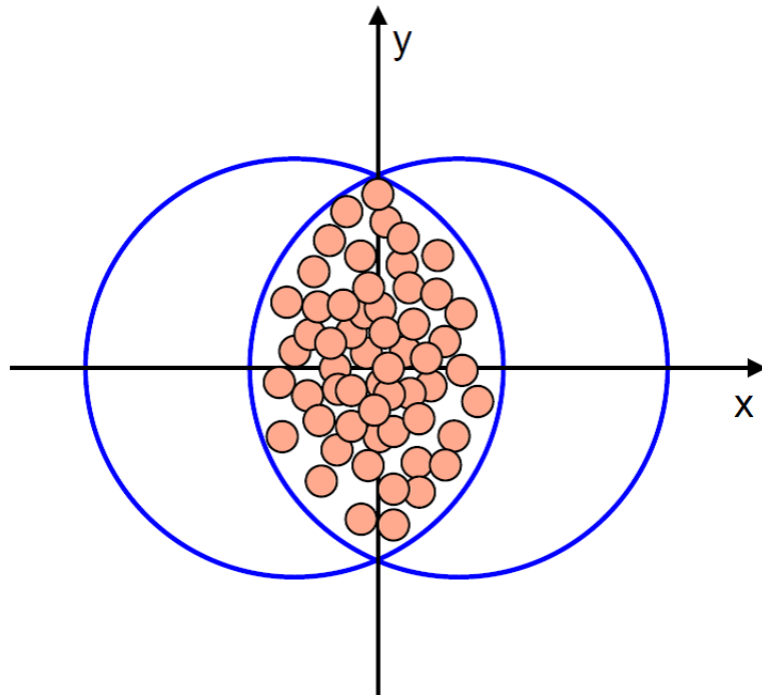


Figure 3.13: Sketch of the coordinate system used for the calculation. The big circles indicate the two Au nuclei in the transverse plane. The impact parameter is parallel to the x axis. The participating nucleons are depicted as filled disks [19].

3.4.3 GEANT Simulation

The PHENIX Integrated Simulation Application (PISA) is a GEANT3-based simulation code. The main inputs to PISA are the event selection, the detector geometry setup for the active and passive volumes, and the tracking criteria. The PISA input file also specifies the various options for the interaction types, energy thresholds, and active detector elements, etc. The GEANT software is then used to track the primary particles and their secondaries within an event. When these particles pass through the selected active detector subsystem, specific hit output data structures are filled during the event. When all particles and secondaries in the event have been tracked until they are stopped or escape the detector volume, then the stored hits are written to an output file called by "PISA hit file". From PISA hit file, the PRDF file is output by using event reconstructing code. Since PISA hit file has the information of tracking for all primary and secondary particles, it can be calculated the total length of track passing through detector element. In the case of BBC, element is the Quarts and interaction type is Cerenkov radiation. Using calibration constants obtained from real data, ADC and TDC output values are calculated by length of track and timing of first incident particles, respectively. Then their values are output to PRDF file. From PISA hit file, primary ancestry file is also generated. Ancestry file is used for estimation of number primary charged particles per pseudo-rapidity. PRDF file is used for obtaining the number of detected charged particles.

3.5 Measurement of Charged Particle Multiplicity

3.5.1 Pseudo-Rapidity Distribution

From simulation data, the conversion factor, which can convert from number of detected charged particles to multiplicity of primary charged particles, is obtained. BBC has six groups of radius from beam pipe to each PMT center position in each side. Rapidity coverage changes with collision vertex point. Thus, conversion factors are obtained for each radii groups and each vertex region. When collision vertex is zero, the difference of rapidity coverage between the radii groups is about 0.2, and when collision vertex shift 2.5cm, the difference of coverage for one radii group is 0.043. 3.14 shows the shift

of each 32 PMTs rapidity coverage when vertex shift $\pm 2.5\text{cm}$. As seen in 3.14, 7 PMT groups are completely separated about its rapidity coverage. 3.15 indicates the 7 PMT groups identified by color, which consists the color in 3.14 and also has same radius from center of PMT to beam pipe. Therefore, the collision vertex will be separated in 5cm, thus 7 groups of a vertex region, and radii group of PMT will be separated by 14 groups, north and south PMT is separated by 7 groups, respectively. Using the ancestry file, I count the number of primary charged particles for each group. For each group, number of detected charged particles is counted by summing whole PMT included same group. After two dimensional histograms between number of detected charged particles and primary charged particles are obtained, liner function is fitted to histogram under assumption that its scatter plot is liner as shown in Figure 3.16. Using event data, number of detected charged particles is obtained in same way written in above, which is separated by collision centrality as shown in Figure 3.17, then, using fitted liner function, number of detected charged particles is corrected to $dN_{ch}/d\eta$. The distribution of number of detected charged particles separated by collision centrality is known by negative binomial distribution (NBD). The mean value of NBD is simple average of distribution, so that the number of detected charged particles indicates simple mean values. Standard error of the mean (SEM) is estimated by root mean square (RMS) of distribution divided by square root of number of entries of distribution. As statistical error, error propagation of SDM and fitting error is calculated. Finally, $dN_{ch}/d\eta$ is obtained for eight rapidity regions by taking an average, which has bin width of 0.2. As systematic error, deviation between average value and each mean value is applied.

3.5.2 Total Multiplicity

In [20], the rapidity distribution of multiplicity of charged particles has been explained using a stochastic approach based on the Ornstein-Uhlenbeck (OU) process with the evolution parameter t , the frictional coefficient γ and the variance σ^2 , described by the partial differential equation;

$$\frac{\partial P(y, t)}{\partial t} = \gamma \left\{ \frac{\partial}{\partial y} y + \frac{1}{2} \frac{\sigma^2}{\gamma} \frac{\partial^2}{\partial y^2} \right\} P(y, t) \quad (3.7)$$

Introducing two sources at $y_{max} = \ln(\sqrt{s_{NN}}/m_N)$ at $t = 0$ and setting $P(y, 0) = 0.5\{\delta(y + y_{max}) + \delta(y - y_{max})\}$, we obtain the distribution func-

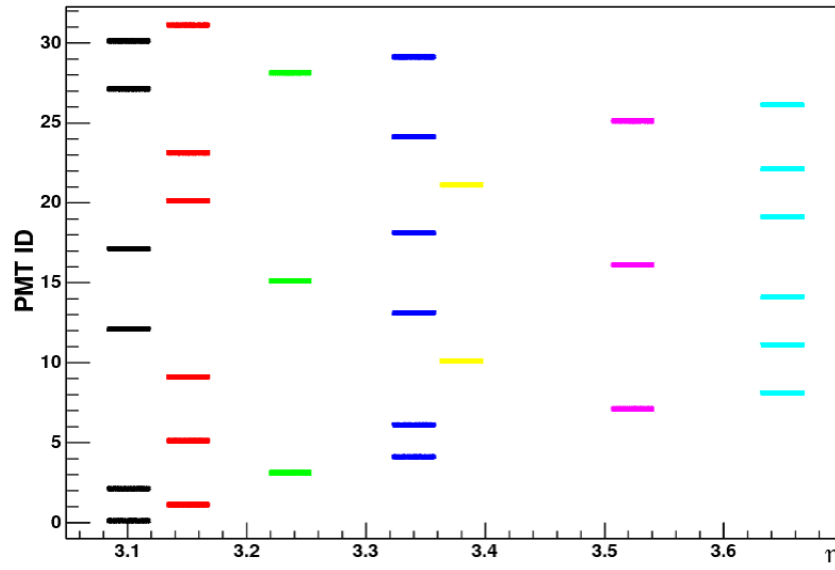


Figure 3.14: The demonstrated histogram of pseudo-rapidity coverage for each PMT. The vertex position is shift $\pm 2.5cm$ around the zero. The group of having same color belongs the group of having same radius.

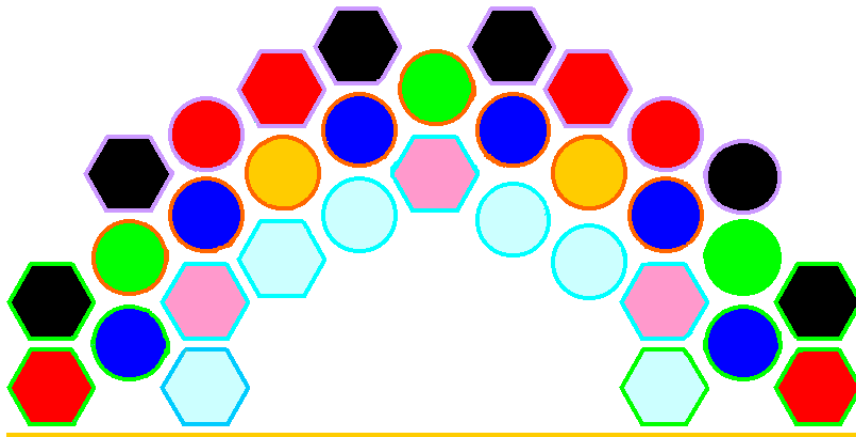


Figure 3.15: The drawings of color separated PMT groups having same radius. These colors correspond to which is shown in 3.14.

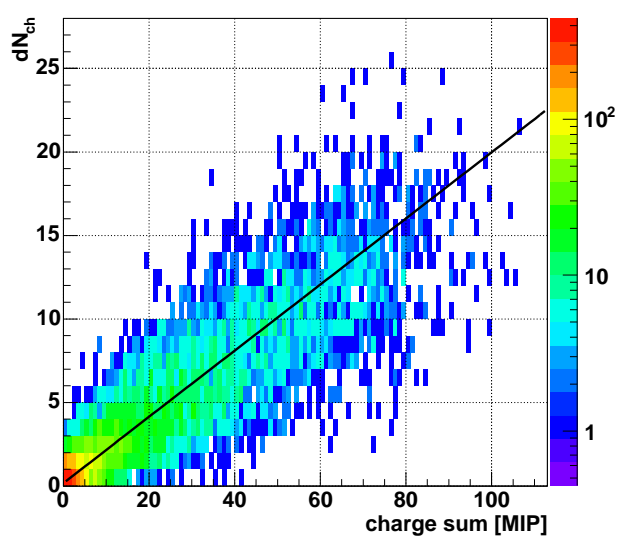


Figure 3.16: Scatter plot between multiplicity of primary charged particle and number of charged particles detected by BBC. Black line shows fit linear function. Conversion factors are determined by fit parameter of linear function.

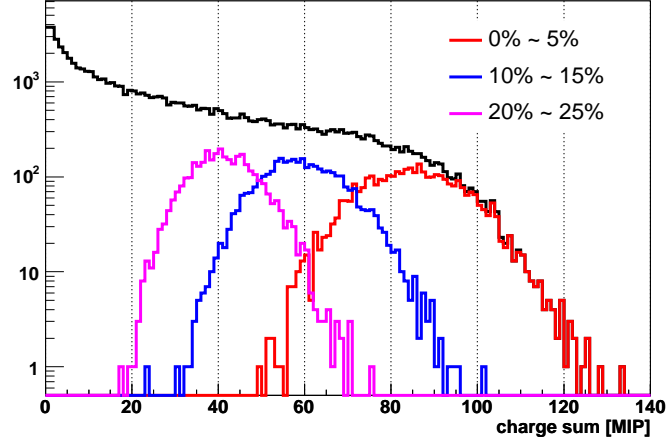


Figure 3.17: Charge sum distribution of BBC. NBD separated by color shows charge sum distribution selected by using centrality class. Simple mean and RMS is applied for data point after correction.

tion for $dN/d\eta$, which derives the symmetric double Gaussian distribution at $\eta = 0$:

$$\frac{dN_{ch}}{d\eta} = p_0 \times \exp\left(-\frac{(x - p_1)^2}{2 \times p_2^2}\right) + p_0 \times \exp\left(-\frac{(-x - p_1)^2}{2 \times p_2^2}\right) \quad (3.8)$$

where p_0 , p_1 , and p_2 is parameters. Double Gaussian distribution is fitted to rapidity distribution in order to interpolate and extrapolate the data point. Then integration over whole rapidity region is carried out so that total multiplicity of primary charged particles as shown in Figure 3.18. Fitting ambiguity is applied as systematic errors of total multiplicity as a function of collision centrality.

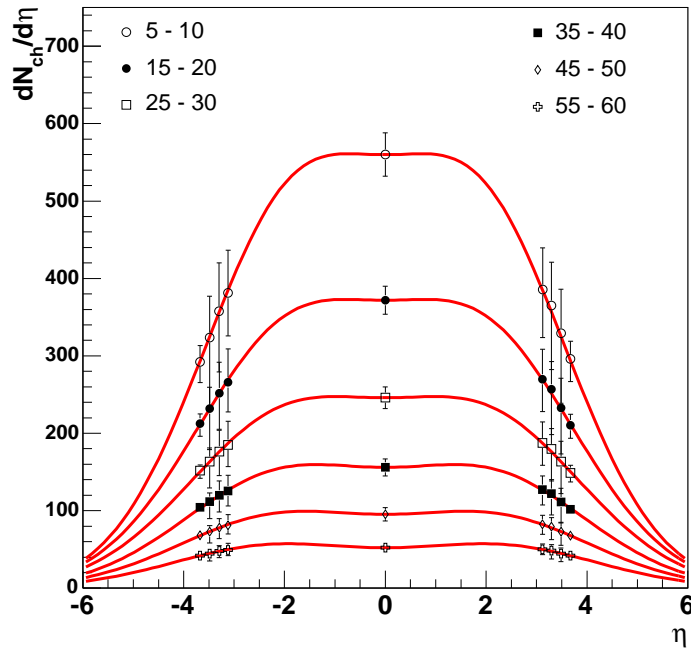
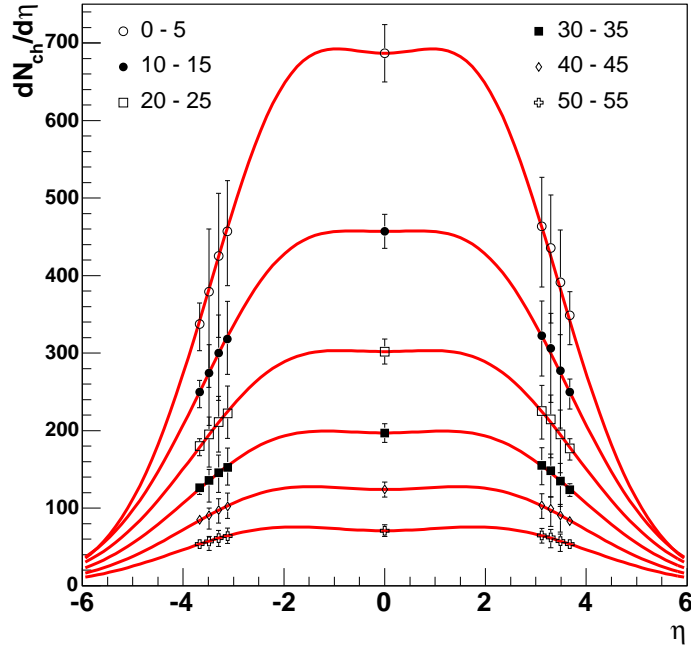


Figure 3.18: Pseudo-rapidity distribution of primary multiplicity of charged particles. Red line shows double Gaussian function fit to the data point. Twelve centrality classes are separated, which is shown by difference of marker style.

Chapter 4

Results and Discussions

4.1 Collision Centrality Scaling

In Figure 4.1, $N_{ch}/(N_{part}/2)$ is shown for this work as a function of N_{part} . It was found that $N_{ch}/(N_{part}/2)$ in Au+Au central collision scales to which in e^+e^- collision. Also it was found that in peripheral Au+Au collision, $N_{ch}/(N_{part}/2)$ does not scale to both which in $pp/\bar{p}p$ collisions and e^+e^- collision. The decreasing of $N_{ch}/(N_{part}/2)$ can be naively understood that the "leading" parton effect comes to appear toward the peripheral collision. This may be not surprising because peripheral collision becomes more closely to the pp collision rather than e^+e^- collision. No "leading" parton effect in central collision suggests that there is no energy dissipation, thus, collision energies carried into the interaction region are exhaustively used for particle production. And this is occurred by results of multiple scattering between incoming nucleons.

4.2 Collision Energy Scaling

In Figure 4.2a, the data on N_{ch} from $pp/\bar{p}p$, e^+e^- and central heavy ion collisions scaled by $N_{part}/2$ are plotted as a function of collision energy. $pp/\bar{p}p$, e^+e^- data and errors are taken from a compilation [21]. The errors are the quadratically combined statistical and systematic errors. Heavy ion data are shown for central Au+Au collision at RHIC ($\sqrt{s_{NN}} = 200GeV$, this work), Au+Au collision from PHOBOS at the RHIC ($\sqrt{s_{NN}} = 130, 56$ and $19.6GeV$), Au+Au collision from E895 at the AGS ($\sqrt{s_{NN}} = 2.6 \sim 4.3GeV$) and Pb+Pb

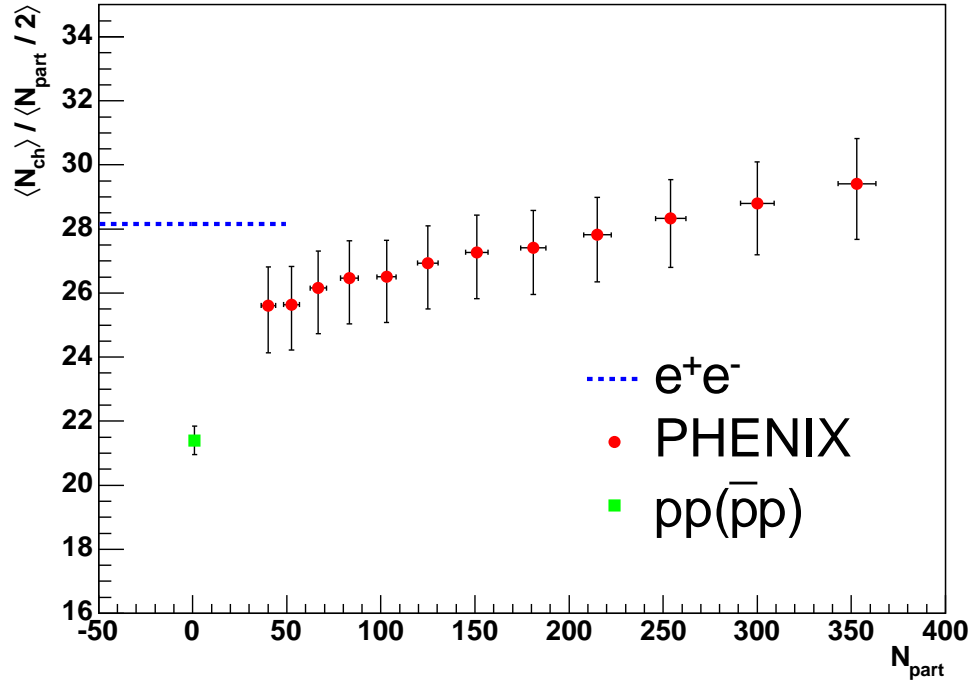


Figure 4.1: The total charged multiplicity scaled by number of participants pair as a function of number of participants for Au+Au collision at $\sqrt{s_{NN}} = 200 \text{ GeV}$. The green box shows pp data at $\sqrt{s_{NN}} = 200 \text{ GeV}$. The dotted line shows the values from the e^+e^- .

collision from NA49 at the SPS ($\sqrt{s_{NN}} = 8.6, 12.2, 17.3\text{GeV}$). All of the errors shown for the heavy ion data are systematic. Perturbative QCD calculations are able to predict the dependence of averaged multiplicity in e^+e^- collisions as a function of $\sqrt{s_{NN}}$ [23]. A fit to the e^+e^- data has been used to Figure 4.2b to see how the various systems compare with e^+e^- data by scaling all of the data at a given $\sqrt{s_{NN}}$. Figure 4.2b shows that the average multiplicity in $pp/\bar{p}p$ collisions is below which in e^+e^- data but having the same slope between e^+e^- data and $pp/\bar{p}p$ data. From the results in measurements of leading partons in pp collisions, dN/dx_F where $x_F = 2p_z/\sqrt{s}$ in the collider reference frame is approximately constant for non diffractive events over a large range of \sqrt{s} [22] and $x_F \sim 0.5$. Therefore, rescaling the \sqrt{s} of each point by a factor of 0.5, brings the data into agreement with the e^+e^- data. Differently from pp data, heavy ion data are reasonable agreement with the e^+e^- data above top SPS energy in no correction of "leading" effect.

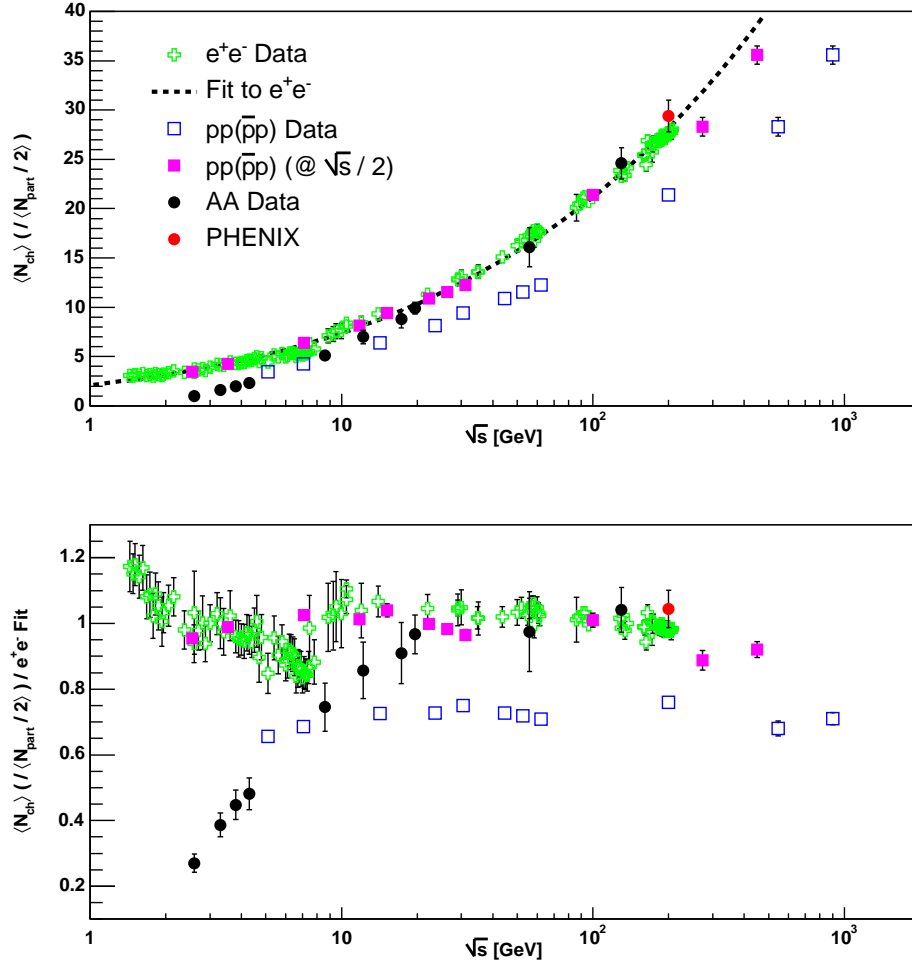


Figure 4.2: (a) The total multiplicity of charged particles for pp , $\bar{p}p$, e^+e^- , and central nucleus-nucleus collisions scaled by number of participants pair as a function of collision energy. The dotted line is a perturbative QCD expression fit to the e^+e^- data. The pink box shows the $pp/\bar{p}p$ data corrected of "leading" parton effect. (b) The data in (a) figure divided by pQCD fit.

Chapter 5

Conclusion

The pseudo-rapidity distribution of multiplicity of primary charged particles as a function of collision centrality in Au+Au collisions at $\sqrt{s_{NN}} = 200\text{GeV}$ was obtained. The total multiplicity per number of nucleon pairs participating to a collision ($N_{ch}/(N_{part}/2)$) was obtained as a function of N_{part} . $N_{ch}/(N_{part}/2)$ in $\sqrt{s_{NN}} = 200\text{GeV}$ was compared with e^+e^- and $pp/\bar{p}p$ data in same \sqrt{s} as a function of N_{part} . It is found that in peripheral collisions, $N_{ch}/(N_{part}/2)$ corresponds to neither e^+e^- nor $pp/\bar{p}p$ collisions. However, in central collisions it is found that $N_{ch}/(N_{part}/2)$ corresponds in the same way of e^+e^- data. This indicates that there are no leading parton effect in central collisions which is observed in $pp/\bar{p}p$ collisions. This leads to the interpretations that all collision energies carried into interactions are consumed for particle productions without dissipations. This implies that multiple scattering is occurring in high energy heavy ion collisions. In addition to $N_{ch}/(N_{part}/2)$ in central Au+Au collision at $\sqrt{s_{NN}} = 200\text{GeV}$, other experimental data in central nuclear-nuclear collisions are compared with e^+e^- and $pp/\bar{p}p$ data in wide center of mass energy range. Above $\sqrt{s} = 20\text{GeV}$, average multiplicity in e^+e^- collision can be well described by pQCD and this shows that the freedom of parton appears in such energy regions. The comparison as a function of collision energy elucidate that $N_{ch}/(N_{part}/2)$ in heavy ion collision above $\sqrt{s_{NN}} = 20\text{GeV}$ scales to e^+e^- data with no correction of leading parton effect. This leads to a picture that in high energy heavy ion collision, especially above $\sqrt{s_{NN}} = 20\text{GeV}$, carriers of particle production is believed to be partons.

In summary, high energy nuclear-nuclear interaction looks like the partons are freely interact each other having longer mean free path than the ordinary

nucleon size. This is not contradictory with a picture of the deconfinement.

Acknowledgement

I first would like to express my great gratitude to Prof. T. Sugitate of Hiroshima University. I would like to express my great gratitude to Prof. K. Shigaki and Dr. K. Homma for their educational suggestions. I also would like to express my great gratitude to T. Nakamura, Y. Tsuchimoto, K. Hosokawa, H. Harada, Y. Nakamiya and H. Sakata

Bibliography

- [1] G. F. Chapline, M. H. Johnson, E. Teller, and M. S. Weiss. Highly excited nuclear matter. *Phys. Rev.*, D8:4302-4308 (1973)
- [2] T. D. Lee and G. C. Wick. Vacuum stability and vacuum excitation in a spic 0 field theory. *Phys. Rev.*, D9:2291 (1974)
- [3] T. D. Lee. Abnormal nuclear states and vacuum excitations. *Rev. Mod. Phys.*, 47:267 (1975)
- [4] John C. Collins and M. J. Perry. Superdense matter: Neutrons or asymptotically free quarks. *Phys. Rev. Lett.*, 34:1353 (1975)
- [5] Z. Fodor, S. D. Katz. *JHEP* 0203 (2002) 014; hep-lat/0106002
- [6] Y. L. Dokshitzer, V. A. Khoze, A. H. Mueller and S. I. Troian, "Basics Of Perturbative QCD," Gif-sur-Yvette, France: Ed. Frontieres (1991)
- [7] PYTHIA manual, T. Sjostrand, *Computer Physics Commun.*, 82:74 (1994)
- [8] M. Basile et al., *Phys. Lett.*, B92:367 (1980)
- [9] M. Basile et al., *Phys. Lett.*, B95:311 (1980)
- [10] J. E. Elias et al., *Phys. Rev. Lett.*, 41:285 (1978)
- [11] A. Bialas, B. Bleszynski, and W. Czyz, *Nucl. Phys.*, B111:461 (1976)
- [12] S. S. Adler et al., *Phys. Rev.* C71:034908 (2005)
- [13] A. Enokizono "Space-time evolution of hot and dense matter probed by Bose-Einstein correlation in Au+Au collisions at $\sqrt{s_{NN}} = 200\text{GeV}$ ".

- [14] <http://www.phenix.bnl.gov/phenix/WWW/magnet/FIGS/Engineering>
- [15] <http://www.phenix.bnl.gov/WWW/run/drawing>
- [16] <http://www.hepl.hiroshima-u.ac.jp/phx/fotolib/detector/.catalogimages>
- [17] http://www.phenix.bnl.gov/phenix/WWW/run/04/subsys_tutorials/zdc
- [18] K. Homma et al., BBC Calibration Status in Y2. (2001)
- [19] K. Reygers. Glauber Monte-Carlo Calculations for Au+Au Collisions at $\sqrt{s_{NN}} = 200\text{GeV}$ (2003)
- [20] M. Biyajima, T. Mizoguchi, Prog. Theor. Phys., 109:483 (2003)
- [21] D. E. Groon et al., Eur. Phys. C33:1 (1986)
- [22] M. Batista and R. J. M. Covelan, Phys. Rev. D59:054006 (1999)
- [23] Ch. Berger et al., Phys. Lett. B95:2 (1980)